



Since January 2020 Elsevier has created a COVID-19 resource centre with free information in English and Mandarin on the novel coronavirus COVID-19. The COVID-19 resource centre is hosted on Elsevier Connect, the company's public news and information website.

Elsevier hereby grants permission to make all its COVID-19-related research that is available on the COVID-19 resource centre - including this research content - immediately available in PubMed Central and other publicly funded repositories, such as the WHO COVID database with rights for unrestricted research re-use and analyses in any form or by any means with acknowledgement of the original source. These permissions are granted for free by Elsevier for as long as the COVID-19 resource centre remains active.



SHORT COMMUNICATION

Molecular Profiling of Coronavirus Disease 2019 (COVID-19) Autopsies Uncovers Novel Disease Mechanisms



Elisabet Pujadas,* Michael Beaumont,[†] Hardik Shah,[†] Nadine Schrode,[†] Nancy Francoeur,[†] Sanjana Shroff,[†] Clare Bryce,* Zachary Grimes,* Jill Gregory,[‡] Ryan Donnelly,* Mary E. Fowkes,* Kristin G. Beaumont,[†] Robert Sebra,^{†§} and Carlos Cordon-Cardo*

From the Department of Pathology, Molecular and Cell-Based Medicine,* and the Department of Genetics and Genomic Sciences,[†] and Academic Informatics and Technology,[‡] Icahn School of Medicine at Mount Sinai, New York, New York; and Sema4,[§] Stamford, Connecticut

Accepted for publication
August 10, 2021.

Address correspondence to
Carlos Cordon-Cardo, M.D.,
Ph.D., Department of Pathology,
Mount Sinai Health System,
One Gustave L. Levy
Place, Box 1194, New York,
NY 10029-6574. E-mail:
carlos.cordon-cardo@mssm.edu.

Current understanding of coronavirus disease 2019 (COVID-19) pathophysiology is limited by disease heterogeneity, complexity, and a paucity of studies assessing patient tissues with advanced molecular tools. Rapid autopsy tissues were evaluated using multiscale, next-generation RNA-sequencing methods (bulk, single-nuclei, and spatial transcriptomics) to provide unprecedented molecular resolution of COVID-19-induced damage. Comparison of infected/uninfected tissues revealed four major regulatory pathways. Effectors within these pathways could constitute novel therapeutic targets, including the complement receptor C3AR1, calcitonin receptor–like receptor, or decorin. Single-nuclei RNA sequencing of olfactory bulb and prefrontal cortex highlighted remarkable diversity of coronavirus receptors. Angiotensin-converting enzyme 2 was rarely expressed, whereas basigin showed diffuse expression, and alanyl aminopeptidase, membrane, was associated with vascular/mesenchymal cell types. Comparison of lung and lymph node tissues from patients with different symptoms (one had died after a month-long hospitalization with multiorgan involvement, and the other had died after a few days of respiratory symptoms) with digital spatial profiling resulted in distinct molecular phenotypes. Evaluation of COVID-19 rapid autopsy tissues with advanced molecular techniques can identify pathways and effectors, map diverse receptors at the single-cell level, and help dissect differences driving diverging clinical courses among individual patients. Extension of this approach to larger data sets will substantially advance the understanding of the mechanisms behind COVID-19 pathophysiology. (*Am J Pathol* 2021, 191: 2064–2071; <https://doi.org/10.1016/j.ajpath.2021.08.009>)

Concerted research efforts are quickly advancing the understanding of coronavirus disease 2019 (COVID-19) pathophysiology, highlighting pathways that influence uncontrolled cytokine release and vascular injury,^{1–3} and suggesting distinct disease stages.⁴ Studies directly evaluating patient tissues,^{5–7} however, often lack the resolution afforded by interrogation with advanced molecular methods. Highly dimensional, patient-specific data sets can be generated through multiscale, next-generation sequencing of well-preserved rapid autopsy tissues. Bulk sequencing yields high-read depth profiling, whereas single-nuclei methods and spatial profiling can interrogate distinct cellular

subpopulations. Mining of such data sets can facilitate novel hypothesis generation, thus advancing the molecular understanding of severe acute respiratory syndrome coronavirus 2 (SARS-CoV-2) infection and COVID-19 mechanisms.

Supported by the Department of Pathology, Molecular and Cell-Based Medicine and the Department of Genetics and Genomic Sciences at the Icahn School of Medicine at Mount Sinai.

E.P. and M.B. contributed equally to this work.

R.S. and C.C.-C. contributed equally to this work as senior authors.

The author M.E.F. is deceased.

Disclosures: R.S. is vice president of technology development at Sema4 (Stamford, CT), a Mount Sinai venture.

Materials and Methods

Clinical Information and Tissue Collection

Rapid autopsies (post-mortem interval of 6 hours) were performed on two decedents (Patient 1 and Patient 2) with appropriate consent and following COVID-19 safety protocols as part of the Mount Sinai COVID-19 autopsy study cohort.⁸ Patient 1 was a man in his 60s with a complex medical history, including well-controlled HIV, organ transplantation, and head and neck squamous cell carcinoma in clinical remission (with no evidence of residual disease at autopsy) who was admitted for treatment of COVID-19 at Mount Sinai Hospital after experiencing fevers for over a week and shortness of breath for 3 days. The hospital admission for Patient 1 lasted over a month and was complicated by hyperinflammatory, hypercoagulable, and cardiac symptoms, leading to multiorgan failure. Patient 2, also a man in his 60s, had diabetes and heart failure and was admitted following 3 days of shortness of breath and no fevers. Patient 2 did not wish to be intubated. His respiratory status continued to decline, and he died shortly after admission. Fresh tissues were frozen on dry ice and stored at -80°C . Formalin-fixed, paraffin-embedded tissues were collected and processed following routine protocols.

Bulk RNA Sequencing and Gene Set Enrichment Analysis

Bulk RNA sequencing (Illumina, San Diego, CA) was performed on two technical replicates across 10 tissues harvested from a single rapid autopsy (Patient 1). The raw RNA-sequencing data were aligned to the hg38 genome using the STAR mapper version 2.7.3a,⁹ annotated using GENCODE v35 gene annotations,¹⁰ and counted using featureCounts version 1.6.3.¹¹ Genes with <50 counts across all samples were excluded from the analysis, and the counts were subsequently \log_2 transformed for differential gene expression analysis using DESeq2 version 1.32.0.¹² The SARS-CoV-2 reference genome employed herein can be found in Global Initiative on Sharing Avian Influenza Data (GISAID, <https://www.gisaid.org>) under accession EPI_ISL_414476. A pairwise comparison between infected tissues (lung and nasopharynx) and uninfected tissues (olfactory bulb, prefrontal cortex, oropharynx, salivary gland, tongue, heart, liver, and kidney) resulted in 4376 differentially expressed genes with a false discovery rate < 0.05 . To assess the biological significance of the differentially expressed genes, a Gene Set Enrichment Analysis (clusterProfiler version 4.0.2¹³) was performed to probe for Gene Ontology (GO) categories that were significantly overrepresented and statistically different in infected versus noninfected tissues. The top four (false discovery rate < 0.05) connected GO categories were plotted as a network linking genes to biological functions and revealed cell activation (green), structure and degradation (purple), cytokine production (blue), and blood vessel

development (red) as overrepresented pathways. Large gray nodes represent GO term biological processes, and smaller nodes represent differentially expressed genes in infected versus uninfected tissues and are shaded according to fold change size.

Single-Nuclei Isolation and snRNA Sequencing of Olfactory Bulb and Prefrontal Cortex Tissues

Nuclei were isolated from frozen tissue following the recommended protocol from 10x Genomics (Pleasanton, CA). In short, lysis buffer (10 mmol/L Tris-HCl, 10 mmol/L NaCl, 3 mmol/L MgCl_2 , and 0.1% Nonidet P40 substitute in nuclease-free water) was added to frozen tissue, which was gently homogenized. Following centrifugation, nuclei were washed in phosphate-buffered saline + 0.04% bovine serum albumin and strained to remove aggregates. Single-nuclei RNA sequencing was performed on these samples using the Chromium platform (10x Genomics) with the 3' gene expression V3 kit, and an input of approximately 10,000 nuclei from a debris-free suspension. Briefly, Gel Bead-in-Emulsions (GEMs) were generated on the sample chip in the Chromium controller. Barcoded cDNA was extracted from the GEMs by post GEM-reverse transcription cleanup and amplified for 12 cycles, followed by fragmentation of amplified cDNA, end repair, poly A-tailing, adapter ligation, and $10\times$ -specific sample indexing, following the manufacturer's protocol. Libraries were quantified using QuBit (ThermoFisher, Waltham, MA) and Bioanalyzer (Agilent, Santa Clara, CA). Libraries were sequenced in paired end mode on a NovaSeq instrument (Illumina) targeting a depth of 50,000 to 100,000 reads per nucleus. The Cell Ranger Single-Cell Software Suite version 3.1 (10x Genomics) was used to align and quantify sequencing data against the provided GRCh38 human reference genome. Downstream analyses, such as graph-based clustering and differential expression analysis/visualization were performed using the Loupe Cell Browser version 3.0 (10x Genomics). Count matrices of all samples were imported and prepared using the R Seurat package version 3.5.3.¹⁴ Quality control for doublets and low-quality cells was achieved through exclusion of cells with <200 or >5000 transcripts and those with a $>20\%$ mitochondrial gene contribution, respectively. Count data were \log normalized and transcripts were scaled and centered, using built-in Seurat functions. Then, filtered and normalized counts of all samples were merged using the Seurat-specific *merge()* function.

Next, dimensionality reduction and clustering were performed where variable transcripts were calculated on the basis of standardized feature values using observed mean and expected variance of a local polynomial regression model. On the resulting variable transcripts, 20 principal components were computed, which, in turn, were used as input for uniform manifold approximation and projection dimensionality reduction. For clustering analysis, a shared nearest neighbor graph was performed, and the modularity function was optimized using the Leiden algorithm. Last,

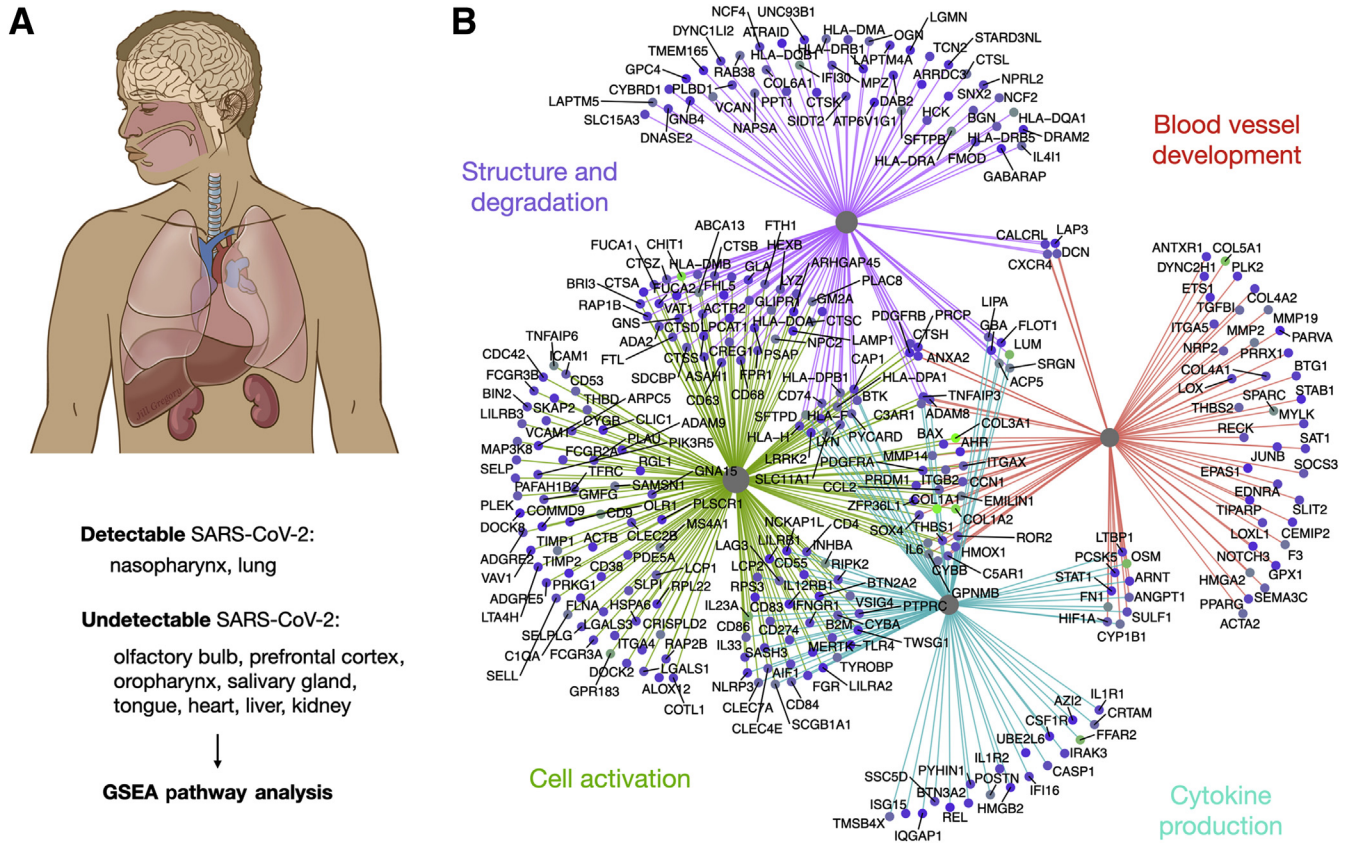


Figure 1 Bulk RNA-sequencing and Gene Set Enrichment Analysis (GSEA) pathway analysis. **A:** Samples from multiple organs were collected at the time of autopsy for Patient 1, a man in his 60s with a complex medical history and a long disease course. Reads mapping to the SARS-CoV-2 genome in unenriched host tissue were detected in nasopharynx and lung, whereas no reads were detected in olfactory bulb, prefrontal cortex, oropharynx, salivary gland, tongue, heart, liver, or kidney. Organ-specific data sets were grouped by infected-uninfected status for further analysis. **B:** Visualization of GSEA, showing the top four most statistically significant pathways. Nodes represent specific transcripts, and edges are color coded to reflect the pathways where the node is enriched. Nodes can have edges from multiple pathways. Illustration in **A** by Jill Gregory, reprinted with permission from © Mount Sinai Health System.

cell types were identified and annotated automatically through machine learning using the singleCellNet R package version 0.1.0,¹⁵ as described in the developer’s manual. Briefly, a random forest classifier was trained on a small conditional RNA-sequencing data set of olfactory neuroepithelium from a healthy donor following cell type annotation¹⁶ and assessed on a withheld subset thereof. The classifier was then applied to the current data set, and a cell type was predicted for each cell.

Digital Spatial Profiling Data Generation and Annotation

Unstained sections were freshly cut from formalin-fixed, paraffin-embedded blocks (4 μm thick) onto positively charged slides and stored at 4°C; immunofluorescence tissue profiling was performed using pan-cytokeratin (488), CD45 (647) leukocyte common antigen, CD68 (568) macrophage marker, and DAPI DNA staining to enable selection of 12 regions of interest (ROIs) for targeted spatial transcriptomics using the commercial platform GeoMx (NanoString, Seattle, WA). ROIs were not divided into specific positive and negative combinations of markers; instead, the markers were used to identify relevant histologic structures

along with composition of inflammatory cells to inform reasonable histologic choices. Circular ROIs measured 600 μm in diameter, and square ROIs measured 600 × 600 μm. The spatial transcriptomic panel included >1600 targeted cancer transcriptome atlas panel with 27 additional SARS-CoV-2 targets added (including ORF1ab and S) to encompass a comprehensive detection of host immune and inflammatory response alongside direct SARS-CoV-2 infection genes. Once digital spatial profiling data quality control was completed, downstream differential expression of six ROIs (three high and three low inflammation) from each patient were concatenated, and differentially expressed genes between patients were determined to demonstrate the ability to differentiate hallmark infection and inflammatory and/or immune response between the two patients in this study. Briefly, reads were processed for high quality with adapter removal, resulting in trimmed reads, and the paired-end reads were merged and aligned. Then, PCR duplicates were removed by matching on the unique molecular index, resulting in deduplicated reads. Quality control (QC) was done in two steps, first segment QC and then biological probe QC. In segment QC, raw read threshold, percentage aligned reads, and technical

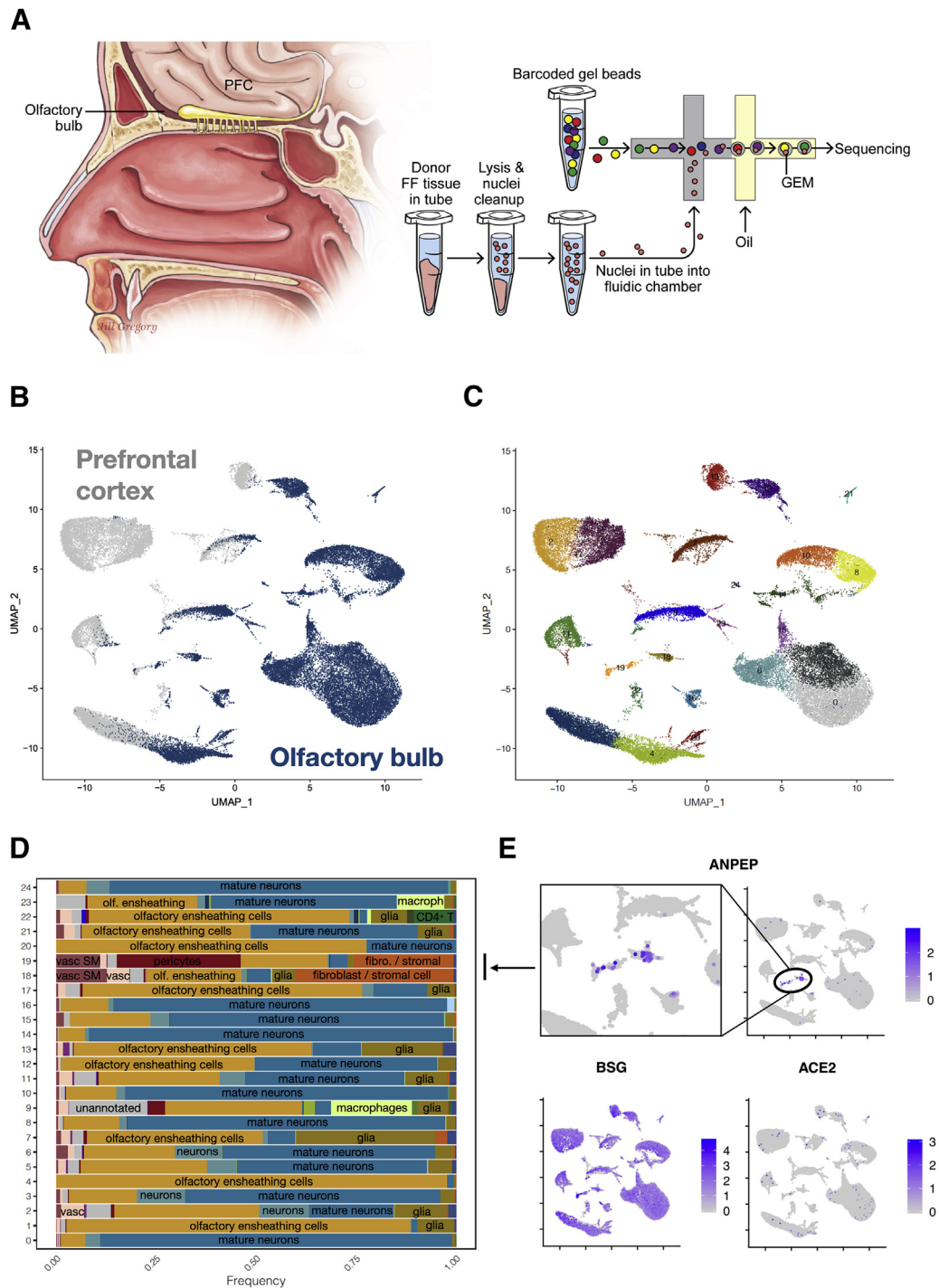


Figure 2 Single-nuclei sequencing of olfactory bulb and prefrontal cortex (PFC). **A: Left side:** Anatomic illustration indicating the location of the olfactory bulb and the overlying PFC collected from Patient 1. Diagram demonstrating 10x Genomics technology for single-nuclei sequencing. **Right side:** Briefly, fresh-frozen (FF) tissue is lysed, and nuclei are cleaned up and flowed into a microfluidic chamber, where they combine with barcoded gel beads to generate gel bead-in-emulsions (GEMs) that are subsequently amplified and sequenced. **B:** Uniform manifold approximation and projection (UMAP) dimensionality reduction graph shows nuclei subpopulations where prefrontal cortex origin is labeled in gray and olfactory bulb origin is labeled in navy blue, showing anatomically distinct subcompartments as well as clusters with a mixture of cell populations. **C:** UMAP dimensionality reduction graph illustrating 25 distinct nuclei subpopulations based on their transcriptional profiles. **D:** Cell types for each nuclei subpopulation were annotated using machine learning. The x axis shows the frequency of each annotated cell type, whereas the y axis has each distinct nuclei subpopulation shown in **B** and **C**. As expected, given the anatomic source of these tissues, most cell types fall under the categories of olfactory ensheathing cells, neurons, and mature neurons. There are also less frequent but important cell types, such as glia, macrophages, $CD4^+$ T lymphocytes, fibroblast and stromal cells, vascular cells, vascular smooth muscle (SM) cells, and pericytes. **E:** Exploration of the expression of coronavirus-related receptors *ACE2* (**bottom right panel**), *BSG* (**bottom left panel**), and *ANPEP* (**top panels**), with a higher-power view of *ANPEP* in clusters 18 and 19 (**top left panel**). The arrow connects the two highlighted clusters (18 and 19) with increased expression of *ANPEP* with their annotation in **D**. Illustration in **A** by Jill Gregory, reprinted with permission from © Mount Sinai Health System.

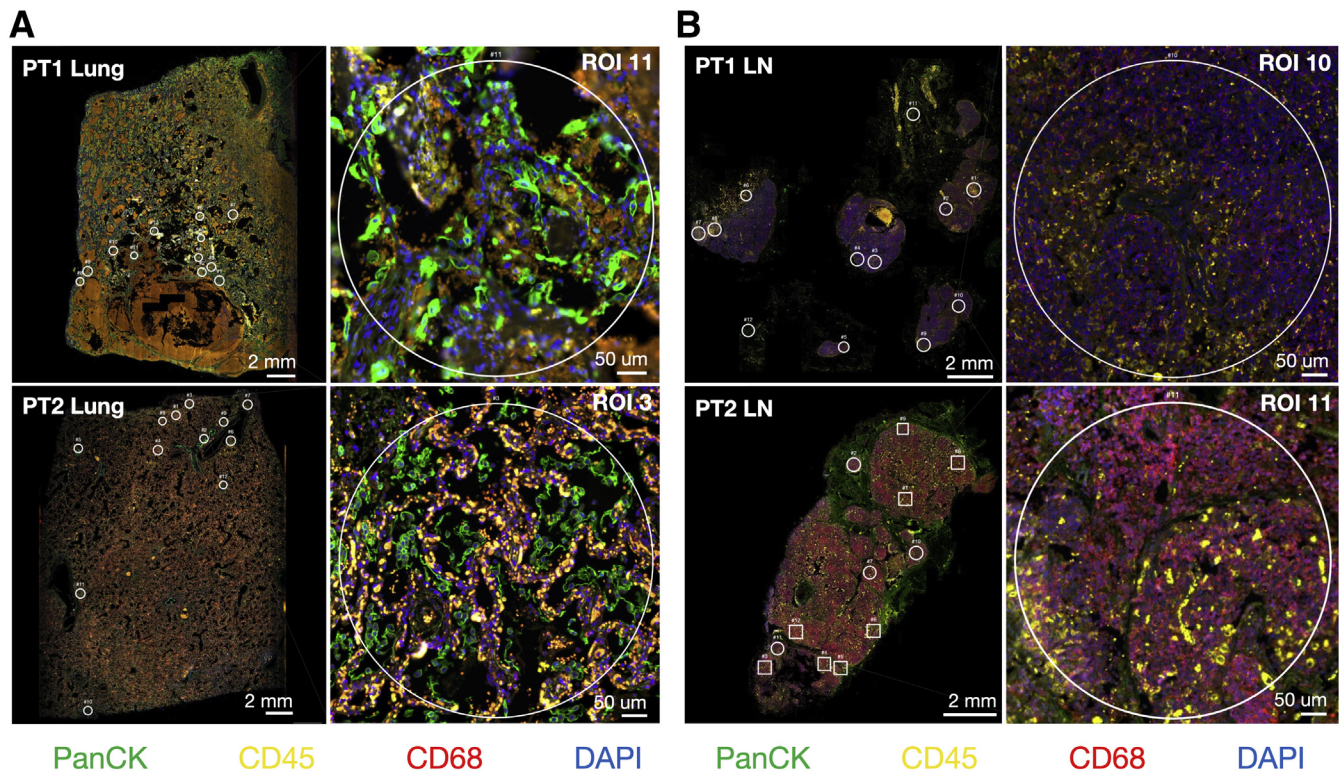


Figure 3 Digital spatial profiling of lung and lymph nodes from Patients 1 and 2. **A:** Whole slide images of immunostained formalin-fixed, paraffin-embedded (FFPE) lung sections from Patient 1 (**top left panel**) and Patient 2 (**bottom left panel**). Small circles denote selected regions of interest (ROIs). Representative ROIs are highlighted: ROI 11 from Patient 1 (**top right panel**) and ROI 3 from Patient 2 (**bottom right panel**). **B:** Whole slide images of immunostained FFPE lymph node sections from Patient 1 (**top left panel**) and Patient 2 (**bottom left panel**). Small circles and squares denote selected ROIs. Representative ROIs are highlighted: ROI 10 from Patient 1 (**top right panel**) and ROI 11 from Patient 2 (**bottom right panel**). Scale bars: 2 mm (**A and B, left column**); 50 μm (**A and B, right column**). LN, lymph node; PanCK, pan-cytokeratin; PT, patient.

background were compared with an expected range to determine the overall quality of the data. Next, biological probe QC was performed to determine the thresholds for excluding outlier probes. Once all ROIs were processed, the raw counts were upper quartile (Q3) normalized against housekeeping genes by averaging to the geometric mean of the internal spike-in controls by which system variation was accounted for. Desired ROIs were annotated with their inflammatory and pathologic status and grouped. The volcano plot illustration shows results of a paired *t*-test of ROIs from each patient tissue section.

Data Availability

Data sets generated and analyzed in this study have been deposited into the National Center for Biotechnology Information Gene Expression Omnibus (<http://www.ncbi.nlm.nih.gov/geo>) under accession numbers GSE182297, GSE182298, and GSE182299.

Results

Fresh-frozen tissue from several organs was obtained at the time of autopsy for Patient 1, a man in his 60s with a

complex medical history, including HIV, status post-transplant, and cancer in clinical remission, whose COVID-19 hospital admission lasted over a month. Bulk RNA-sequencing evaluation revealed viral RNA in the nasopharynx and lung (148 and 120 reads, respectively, mapping to SARS-CoV-2 reference genome), but not in the olfactory bulb (OB), prefrontal cortex (PFC), oropharynx, salivary gland, tongue, heart, liver, or kidney (**Figure 1A**). Differential gene expression analysis between infected and uninfected tissues resulted in 4376 differentially expressed genes (false discovery rate < 0.05). To assess biological significance, Gene Set Enrichment Analysis was performed to probe for GO categories significantly overrepresented in infected versus uninfected tissues (false discovery rate < 0.05) (**Figure 1B**). The top four connected GO categories include blood vessel development, cytokine production, cell activation, and structure and degradation. All four pathways share TNF- α induced protein 3 (TNFAIP3), complement C3a receptor 1 (C3AR1), and ADAM8, a metalloproteinase involved in leukocyte extravasation. Other examples of conserved molecules across multiple pathways include angiopoietin 1 (ANGPT1), calcitonin receptor–like receptor (CALCRL), and decorin (DCN), an activator of autophagy.

snRNA sequencing was performed on OB and PFC of Patient 1 to highlight functionally significant expression

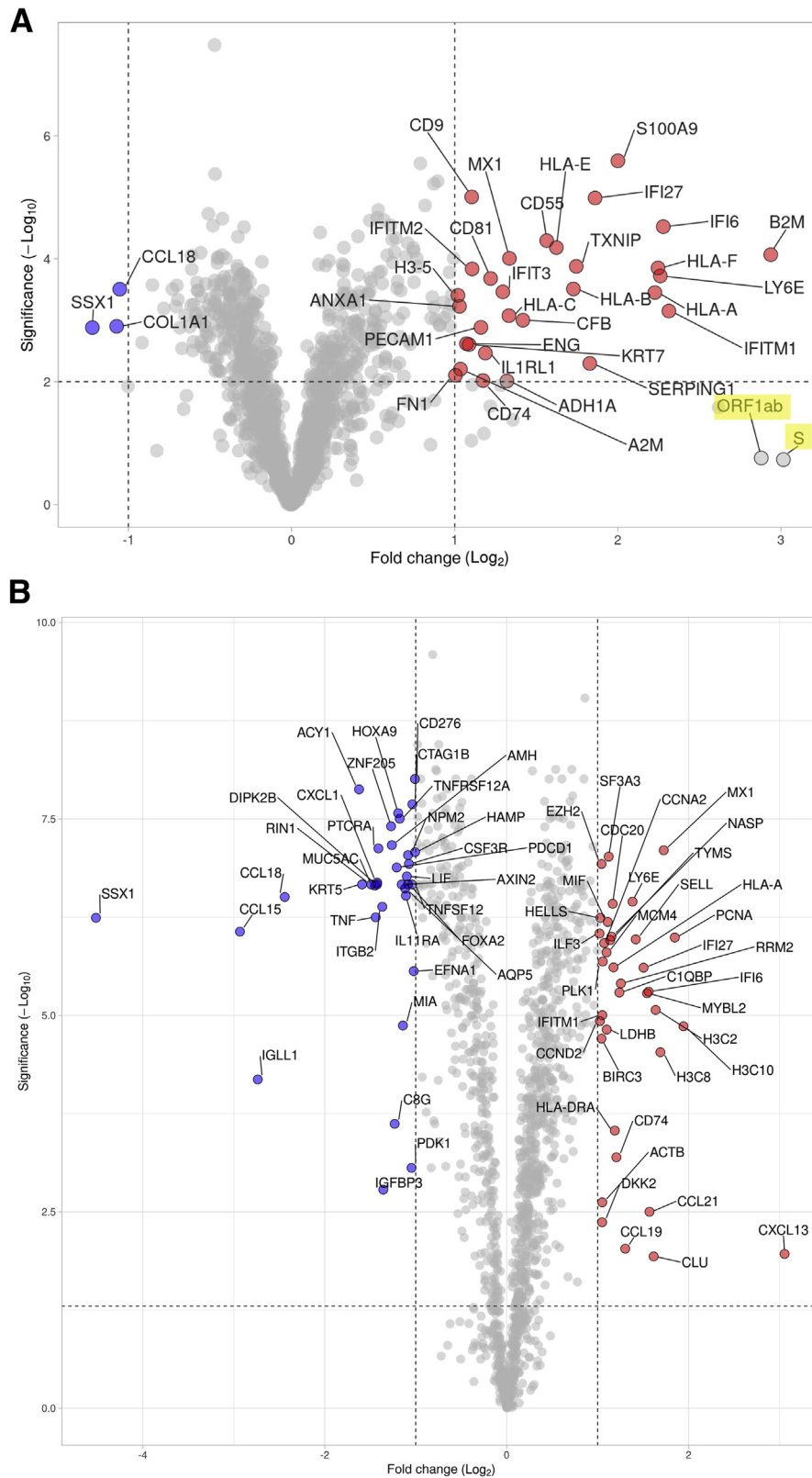


Figure 4 Gene expression differences in lung and lymph node tissues from Patient 1 and Patient 2. **A:** Volcano plot comparing gene expression profiles of selected lung regions of interest (ROIs) between Patient 1 and Patient 2 using the commercial NanoString GeoMx platform. Transcripts labeled in blue are significantly more expressed in Patient 1, whereas transcripts labeled in red are significantly more expressed in Patient 2. Yellow highlights denote viral transcripts. **B:** Volcano plot comparing gene expression profiles of selected lymph node ROIs between Patient 1 and Patient 2 using the commercial NanoString GeoMx platform. Transcripts labeled in blue are significantly more expressed in Patient 1, whereas transcripts labeled in red are significantly more expressed in Patient 2.

heterogeneity within niche cellular compartments (Figure 2A). Dimensionality reduction and clustering showed expected separation between OB and PFC (Figure 2B) and identified 25 unique subpopulations (Figure 2C) that were annotated using existing databases (Figure 2D). Expression levels of any transcript from nuclei within these subpopulations can inform hypotheses unresolvable by bulk RNA analyses. For example, examination of multiple coronavirus-associated receptors reveals only scattered expression of angiotensin-converting enzyme 2 (ACE2) in rare cells and robust expression of basigin (BSG) throughout, whereas alanyl aminopeptidase, membrane (ANPEP) is exclusively expressed in two subpopulations enriched for pericytes and vascular, fibroblastic, and stromal cells (Figure 2E).

Digital spatial profiling was performed on formalin-fixed, paraffin-embedded tissue across multiple organs from two COVID-19 autopsy patients. Patient 1 was as above, and Patient 2 was a man in his 60s with diabetes and heart failure who died after only 3 days of symptoms. Following immunostaining, 12 ROIs per slide (Figure 3) were selected for targeted spatial sequencing. Viral transcripts (ORF1ab and S) were detected in the lungs of Patient 2 (Figure 4A), along with a more robust inflammatory response compared with Patient 1, including higher expression of MX1, an interferon-induced GTPase with antiviral activity against RNA viruses, IL-1 receptor type 1 (IL1R1), and interferon- α inducible protein 6 (IFI6), a negative regulator of apoptosis (Figure 4A). Comparison of lymph node ROIs between these two patients showed diverging inflammatory signatures (Figure 4B). Patient 1 had higher expression of the chemotactic factors CCL15 and CCL18, along with TNF and ITGB2, a receptor for the iC3b complement fragment and fibrinogen, whereas Patient 2 had higher expression of transcripts related to cell proliferation and division, including thymidylate synthetase (TYMS), CCNA2, NASP, lymphocyte antigen 6 family member E (LY6E), and multiple histone subunits (Figure 4B).

Discussion

Multiscale, high-resolution molecular profiling of select tissues from COVID-19 patients, collected at autopsy, demonstrates how these technologies can facilitate hypothesis generation, as evidenced by this and other studies leveraging the power of single-cell and spatial transcriptomic technologies.^{17,18} First, bulk RNA sequencing was employed to evaluate presence of viral RNA across organs from Patient 1. Next, infected and uninfected tissues were compared to determine key regulatory pathways associated with infection, including blood vessel development, cytokine production, cell activation, and structure and degradation. Numerous specific regulators, including C3AR1, a complement receptor controlling neutrophil extracellular trap formation, can lead to a prothrombotic state,¹⁹ both important mechanisms implicated in

COVID-19 progression.⁴ C3AR1 is thus one of many examples that could serve as a valuable target.

Next, snRNA sequencing was performed on OB and PFC tissues from Patient 1 to illustrate the feasibility and importance of mapping expression heterogeneity within cellular niches. Although significant attention has been directed towards ACE2, there are numerous coronavirus-associated receptors.²⁰ ACE2 was rarely expressed in the brain tissues analyzed herein, whereas BSG was more widely expressed, and ANPEP showed preferential expression in vascular cell types, such as endothelial cells and pericytes. Even though Patient 1 had no detectable virus in OB or PFC at the time of autopsy, these results remain important as they provide evidence of infection potential in the brain via alternative receptors. In addition, these findings illustrate how expression heterogeneity in micro-anatomic compartments can underlie systemic, variable host-driven responses affecting uninfected tissues, as may be seen in the context of hyperinflammatory and hypercoagulable syndromes. Understanding the true complexity of SARS-CoV-2 infection and COVID-19 will require careful mapping of all entry receptors and other host regulatory factors in a manner that can resolve each cellular niche.

Last, digital spatial profiling was demonstrated in formalin-fixed, paraffin-embedded tissues, emphasizing the importance of integrating transcriptional profiling with histologic features and microanatomic detail. This technology allows evaluation of a larger sample set, yet still provides viral detection and the ability to compare patients with different characteristics and disease courses. Although many factors could account for the differences seen between these two patients, it is tempting to speculate that some of these findings reflect early versus late-stage COVID-19, in terms of both viral presence and robustness of lymphocytic activation in Patient 2, with a shorter disease course; and phagocytic and coagulopathic signatures in Patient 1, with a prolonged hospitalization and extended organ damage. The limited cohort size and the complexity of the clinical histories preclude further generalization of these findings.

In summary, this work describes four key pathways seen in severe COVID-19 and provides specific effectors for further study as potential diagnostic and therapeutic targets. Single-nuclei technology reveals remarkable heterogeneity of coronavirus receptors within well-defined anatomic compartments, and digital spatial profiling of formalin-fixed tissues reveals diverging molecular signatures between patients with different clinical courses. These findings, although limited by small sample size, underline the need to deploy advanced molecular techniques to dissect the complexity of COVID-19 pathophysiology and their promise when applied to much larger patient cohorts.

References

1. Tay MZ, Poh CM, Renia L, MacAry PA, Ng LFP: The trinity of COVID-19: immunity, inflammation and intervention. *Nat Rev Immunol* 2020, 20:363–374

2. Colling ME, Kanthi Y: COVID-19-associated coagulopathy: an exploration of mechanisms. *Vasc Med* 2020, 25:471–478
3. Gupta A, Madhavan MV, Sehgal K, Nair N, Mahajan S, Sehrawat TS, Bikdeli B, Ahluwalia N, Ausiello JC, Wan EY, Freedberg DE, Kirtane AJ, Parikh SA, Maurer MS, Nordvig AS, Accili D, Bathon JM, Mohan S, Bauer KA, Leon MB, Krumholz HM, Uriel N, Mehra MR, Elkind MSV, Stone GW, Schwartz A, Ho DD, Bilezikian JP, Landry DW: Extrapulmonary manifestations of COVID-19. *Nat Med* 2020, 26:1017–1032
4. Cordon-Cardo C, Pujadas E, Wajnberg A, Sebra R, Patel G, Firpo-Betancourt A, Fowkes M, Sordillo E, Paniz-Mondolfi A, Gregory J, Krammer F, Simon V, Isola L, Soon-Shiong P, Aberg JA, Fuster V, Reich DL: COVID-19: staging of a new disease. *Cancer Cell* 2020, 38:594–597
5. Schaefer IM, Padera RF, Solomon IH, Kanjilal S, Hammer MM, Hornick JL, Sholl LM: In situ detection of SARS-CoV-2 in lungs and airways of patients with COVID-19. *Mod Pathol* 2020, 33:2104–2114
6. Puelles VG, Lutgehetmann M, Lindenmeyer MT, Sperhake JP, Wong MN, Allweiss L, Chilla S, Heinemann A, Wanner N, Liu S, Braun F, Lu S, Pfeifferle S, Schroder AS, Edler C, Gross O, Glatzel M, Wichmann D, Wiech T, Kluge S, Pueschel K, Aepfelbacher M, Huber TB: Multiorgan and renal tropism of SARS-CoV-2. *N Engl J Med* 2020, 383:590–592
7. Massoth LR, Desai N, Szabolcs A, Harris CK, Neyaz A, Crotty R, Chebib I, Rivera MN, Sholl LM, Stone JR, Ting DT, Deshpande V: Comparison of RNA in situ hybridization and immunohistochemistry techniques for the detection and localization of SARS-CoV-2 in human tissues. *Am J Surg Pathol* 2021, 45:14–24
8. Bryce C, Grimes Z, Pujadas E, Ahuja S, Beasley MB, Albrecht R, et al: Pathophysiology of SARS-CoV-2: the Mount Sinai COVID-19 autopsy experience. *Mod Pathol* 2021, 34:1456–1467
9. Dobin A, Davis CA, Schlesinger F, Drenkow J, Zaleski C, Jha S, Batut P, Chaisson M, Gingeras TR: STAR: ultrafast universal RNA-seq aligner. *Bioinformatics* 2013, 29:15–21
10. Frankis A, Diekhans M, Ferreira AM, Johnson R, Jungreis I, Loveland J, et al: GENCODE reference annotation for the human and mouse genomes. *Nucleic Acids Res* 2019, 47:D766–D773
11. Liao Y, Smyth GK, Shi Wei: featureCounts: an efficient general-purpose program for assigning sequence reads to genomic features. *Bioinformatics* 2014, 30:923–930
12. Love MI, Huber W, Anders S: Moderated estimation of fold change and dispersion for RNA-seq data with DESeq2. *Genome Biology* 2014, 15:550
13. Wu T, Hu E, Xu S, Chen M, Guo P, Dai Z, Feng T, Zhou L, Tang W, Zhan L, Fu X, Liu S, Bo X, Yu G: clusterProfiler 4.0: A universal enrichment tool for interpreting omics data. *Innovation (N Y)* 2021, 2:100141
14. Butler A, Hoffman P, Smibert P, Papalexi E, Satija R: Integrating single-cell transcriptomic data across different conditions, technologies, and species. *Nat Biotechnol* 2018, 36:411–420
15. Tan Y, Cahan P: SingleCellNet: a computational tool to classify single cell RNA-Seq data across platforms and across species. *Cell Syst* 2019, 9:207–213.e2
16. Durante MA, Kurtenbach S, Sargi ZB, Harbour JW, Choi R, Kurtenbach S, Goss GM, Matsunami H, Goldstein BJ: Single-cell analysis of olfactory neurogenesis and differentiation in adult humans. *Nat Neurosci* 2020, 23:323–326
17. Melms JC, Biermann J, Huang H, Wang Y, Nair A, Tagore S, et al: A molecular single-cell lung atlas of lethal COVID-19. *Nature* 2021, 595:114–119
18. Delorey TM, Ziegler CGK, Heimberg G, Normand R, Yang Y, Segerstolpe A, et al: COVID-19 tissue atlases reveal SARS-CoV-2 pathology and cellular targets. *Nature* 2021, 595:107–113
19. Guglietta S, Chiavelli A, Zagato E, Krieg C, Gandini S, Ravenda PS, Bazolli B, Lu B, Penna G, Rescigno M: Coagulation induced by C3aR-dependent NETosis drives protumorigenic neutrophils during small intestinal tumorigenesis. *Nat Commun* 2016, 7:11037
20. Singh M, Bansal V, Feschotte C: A single-cell RNA expression map of human coronavirus entry factors. *Cell Rep* 2020, 32:108175